Predictions for production of ${}^{3}_{\Lambda}\mathrm{H}$ and ${}^{3}_{\Lambda}\overline{\mathrm{H}}$ in isobaric ${}^{96}_{44}\mathrm{Ru}+{}^{96}_{44}\mathrm{Ru}$ and ${}^{96}_{40}\mathrm{Zr}+{}^{96}_{40}\mathrm{Zr}$ collisions at $\sqrt{s_{NN}}=200$ GeV

Zhi-Lei She,[1,2] Gang Chen,[2,*] Dai-Mei Zhou,[3] Liang Zheng,[2] Yi-Long Xie,[2] and Hong-Ge Xu[2]

[1]*Institute of Geophysics and Geomatics, China University of Geosciences, Wuhan 430074, China*

[2]*School of Mathematics and Physics, China University of Geosciences, Wuhan 430074, China*

[3]*Institute of Particle Physics, Central China Normal University, Wuhan 430079, China*

(Received 23 September 2020; accepted 19 January 2021; published 27 January 2021)

The production of ${}^{3}_{\Lambda}\mathrm{H}$ and ${}^{3}_{\Lambda}\overline{\mathrm{H}}$, as well as ${}^{3}\mathrm{H}$, ${}^{3}\overline{\mathrm{H}}$, ${}^{3}\mathrm{He}$, and ${}^{3}\overline{\mathrm{He}}$ are studied in central collisions of isobars ${}^{96}_{44}\mathrm{Ru}+{}^{96}_{44}\mathrm{Ru}$ and ${}^{96}_{40}\mathrm{Zr}+{}^{96}_{40}\mathrm{Zr}$ at $\sqrt{s_{\mathrm{NN}}}=200$ GeV, using the dynamically constrained phase-space coalescence model and the PACIAE model with chiral magnetic effect. The yield, yield ratio, coalescence parameters, and strangeness population factor of (anti-)hypertriton and (anti-)nuclei produced in isobaric ${}^{96}_{44}\mathrm{Ru}+{}^{96}_{44}\mathrm{Ru}$ and ${}^{96}_{40}\mathrm{Zr}+{}^{96}_{40}\mathrm{Zr}$ collisions are predicted. The (anti-)hypertriton and (anti-)nuclei production is found to be insensitive to the chiral magnetic effects. Experimental data of Cu + Cu, Au + Au, and Pb + Pb collisions from RHIC, LHC, and the results of the PACIAE + DCPC model are presented in the results for comparison.

DOI: 10.1103/PhysRevC.103.014906

I. INTRODUCTION

Hypernuclei and their antihypernuclei are copiously produced under conditions of extreme high temperatures and energy densities in high-energy heavy-ion collisions. It creates a unique opportunity to study whether hypernuclei and antihypernuclei have the same behavior and to investigate the difference between light (anti-)nuclei and (anti-)hypernuclei [1–3]. Hence it attracts a constant interest in studying antimatter and exploring fundamental problems in physics, e.g., testing the fundamental charge-parity-time reversal (CPT) theorem by precisely measuring the difference of the mass, lifetime, and binding energy between hypertriton (${}^{3}_{\Lambda}\mathrm{H}$) and its corresponding antihypertriton (${}^{3}_{\Lambda}\overline{\mathrm{H}}$) [4,5] in Au + Au and Pb + Pb collision systems.

The antihypertriton (${}^{3}_{\Lambda}\overline{\mathrm{H}}$), the lightest bound antihypernucleus, consists of an antihyperon $\overline{\Lambda}$, an antiproton $\overline{p}$, and an antineutron $\overline{n}$, which was discovered in Au + Au collisions at $\sqrt{s_{\mathrm{NN}}}=200$ GeV by the STAR Collaboration at the BNL Relativistic Heavy Ion Collider (RHIC) [6] and then in Pb + Pb collisions at $\sqrt{s_{\mathrm{NN}}}=2.76$ TeV by the ALICE Collaboration at the Large Hadron Collider (LHC) in CERN [7], respectively. The production of ${}^{3}_{\Lambda}\mathrm{H}$ (${}^{3}_{\Lambda}\overline{\mathrm{H}}$) has distinct features in heavy-ion collisions compared with corresponding normal three-body (anti-)nuclei ${}^{3}\mathrm{He}$ (${}^{3}\overline{\mathrm{He}}$) and ${}^{3}\mathrm{H}$ (${}^{3}\overline{\mathrm{H}}$), due to the different interaction strengths between hyperon-nucleon and nucleon-nucleon [8]. Their detailed production mechanism is, however, not fully understood. Hence the related theoretical approaches on production of light (anti-)nuclei and ${}^{3}_{\Lambda}\mathrm{H}$ (${}^{3}_{\Lambda}\overline{\mathrm{H}}$) have been carried out in the frameworks of either the statistical thermal method [9–14] or the coalescence model [15–20].

The existence of ${}^{3}_{\Lambda}\mathrm{H}$ (${}^{3}_{\Lambda}\overline{\mathrm{H}}$) in heavy-ion reactions are observed, ranging from AGS [21] up to RHIC [6,20] and LHC [7] collision energies, involving various collision systems, such as ${}^{63}\mathrm{Cu}+{}^{63}\mathrm{Cu}$, ${}^{197}\mathrm{Au}+{}^{197}\mathrm{Au}$, and ${}^{208}\mathrm{Pb}+{}^{208}\mathrm{Pb}$ collisions. One can see that there exists a gap of the system size for nucleus-nucleus interactions between ${}^{63}\mathrm{Cu}+{}^{63}\mathrm{Cu}$ and ${}^{197}\mathrm{Au}+{}^{197}\mathrm{Au}$ collisions. However, the recent isobar program consisting of ${}^{96}_{44}\mathrm{Ru}+{}^{96}_{44}\mathrm{Ru}$ and ${}^{96}_{40}\mathrm{Zr}+{}^{96}_{40}\mathrm{Zr}$ collisions at the top RHIC energies of $\sqrt{s_{\mathrm{NN}}}=200$ GeV, is favored to search for the presence of the chiral magnetic effect (CME) [22–26], and it can also be used to fill the gap of collision system size discussed above.

The CME effect can reveal some topological and electromagnetic properties of the quark gluon plasma(QGP) in high-energy heavy-ion collisions. Charge separation is an important consequence of the CME. Ma *et al.* [27–30] introduced an additional CME-induced charge separation to the initial conditions obtained from a multiphase transport model(AMPT) [31], to study the CME-related physics. References [27,28] demonstrated that the final-state interactions can reduce the charge separation in each collision, while the relative difference of the CME signal between the two isobaric collisions is insensitive to the final-state interactions.

In this paper, the production of the final-state hadrons, including p, $\overline{p}$, Λ, and $\overline{\Lambda}$, are simulated by the parton and hadron cascade model (PACIAE) [32], and an initial three-flavor dipole charge separation [27] is introduced to simulate the CME, in ${}^{96}_{44}\mathrm{Ru}+{}^{96}_{44}\mathrm{Ru}$ and ${}^{96}_{40}\mathrm{Zr}+{}^{96}_{40}\mathrm{Zr}$ at the top RHIC energy of $\sqrt{s_{\mathrm{NN}}}=200$ GeV with midrapidity ($|\eta|<0.5$). Then, the dynamically constrained phase-space coalescence (DCPC) model [33] is applied to study the production of ${}^{3}_{\Lambda}\mathrm{H}$(${}^{3}_{\Lambda}\overline{\mathrm{H}}$) clusters in these two isobaric collision systems. In this study, we expect to compare and investigate the production and properties of

*chengang1@cug.edu.cn

${}^{3}_{\Lambda}\mathrm{H}$ (${}^{3}_{\Lambda}\overline{\mathrm{H}}$) in ${}^{96}_{44}\mathrm{Ru}+{}^{96}_{44}\mathrm{Ru}$ and ${}^{96}_{40}\mathrm{Zr}+{}^{96}_{40}\mathrm{Zr}$ collision systems involving the chiral magnetic effect.

The paper is organized as follows: In Sec. II, we provide a concise introduction to the PACIAE with CME and DCPC model. Section III contains our numerical calculations for production and properties of ${}^{3}_{\Lambda}\mathrm{H}$ (${}^{3}_{\Lambda}\overline{\mathrm{H}}$). In Sec. IV, a short summary is given.

II. MODELS

The PACIAE model [32] is based on PYTHIA 6.4 [34] and is designed for various collision systems ranging from proton induced reactions ($p+p$ and $p+A$), to nuclear reactions ($A+A$). Generally, this entire model has four main physics stages composed of the parton initiation, parton rescattering, hadronization, and hadron rescattering.

At the first stage, the nucleus-nucleus collision is decomposed into the nucleon-nucleon (NN) collisions according to the collision geometry and NN total cross section. The strings created in the NN collisions will break up into free partons leading to the formation of the deconfined quark-gluon matter. After that, the decomposed partons interact with each other relied on the $2\rightarrow 2$ LO-pQCD parton-parton cross sections [35]. Here, a K factor is added to account for nonperturbative QCD and higher-order corrections. Then, the hadronization conducts via either the Lund string fragmentation model [34] or the phenomenological coalescence model [32]. The last step is the hadron rescattering process happening among the generated hadrons until the hadronic freeze-out. (For more details see Ref. [32].)

To study the CME-related physics, an additional CME-induced charge separation mechanism [27], which switches p_y values for a fraction f of the downward moving $u(\overline{d})$ quarks with those of the upward moving $\overline{u}(d)$ quarks, is needed to introduce into the initial conditions in the original PACIAE model [32]. The fraction f can be described as

$$f=\frac{N^{+(-)}_{\uparrow(\downarrow)}-N^{+(-)}_{\downarrow(\uparrow)}}{N^{+(-)}_{\uparrow(\downarrow)}+N^{+(-)}_{\downarrow(\uparrow)}}, \tag{1}$$

where N denotes the number of a given quark, $+$ and $-$ represent positive and negative charges, $\uparrow$ and $\downarrow$ are the moving directions of quarks along the y axis, respectively. As the Ref. [28] mentioned, the initial charge separation fractions f are different between isobars ${}^{96}_{44}\mathrm{Ru}+{}^{96}_{44}\mathrm{Ru}$ and ${}^{96}_{40}\mathrm{Zr}+{}^{96}_{40}\mathrm{Zr}$ collisions since they have a same nucleon number but the 10% difference in proton number. In this work, we introduce an initial three-flavor quark (u,d,s) charge separation into original PACIAE model [32] to investigate the CME-related physics.

The DCPC model [33] is developed to calculate production of light (anti-)nuclei and (anti-)hypernuclei, after the final-state particles produced by the PACIAE model [32] in high-energy collisions. Previous works of (anti-)nuclei and (anti-)hypernuclei production in different collision systems, e.g., pp [33,36,37], Cu + Cu [20,38], Au + Au [39–42] and Pb + Pb [43,44] interactions, have been studied using the same framework.

According to the quantum statistical mechanics, one can estimate the yield of a single particle in the six-dimensional phase space by an integral

$$Y_1=\int_{H\leqslant E}\frac{d\vec{q}d\vec{p}}{h^3}, \tag{2}$$

where H and E represent the Hamiltonian and energy of the particle, respectively. Similarly, the yield of an N particle cluster can also be computed using the following integral:

$$Y_N=\int\cdots\int_{H\leqslant E}\frac{d\vec{q}_1d\vec{p}_1\cdots d\vec{q}_Nd\vec{p}_N}{h^{3N}}. \tag{3}$$

In addition, equation (3) must meet the following constraint conditions:

$$m_0\leqslant m_{inv}\leqslant m_0+\Delta m, \tag{4}$$

$$|\vec{q}_{ij}|\leqslant D_0\ (i\neq j;\ i,j=1,2,\ldots,N). \tag{5}$$

where

$$m_{inv}=\left[\left(\sum_{i=1}^{N}E_i\right)^2-\left(\sum_{i=1}^{N}\vec{p}_i\right)^2\right]^{1/2}, \tag{6}$$

and E_i, $\vec{p}_i$ $(i=1,2,...,N)$ are the energies and momenta of particles, respectively. m_0 and D_0 denote the rest mass and diameter of light (anti-)nuclei or (anti-)hypernuclei. Here, the radius values $R=1.74, 1.61, 5.0$ fm are chosen for ${}^{3}\mathrm{He}$ (${}^{3}\overline{\mathrm{He}}$), ${}^{3}\mathrm{H}$ (${}^{3}\overline{\mathrm{H}}$), and ${}^{3}_{\Lambda}\mathrm{H}$ (${}^{3}_{\Lambda}\overline{\mathrm{H}}$) [19,21,45] in this simulation, respectively. Δm represents the allowed mass uncertainty, and $|\vec{q}_{ij}|$ presents the distance between particles i and j. The integration in Eq. (3) should be replaced by the summation over discrete distributions, as a coarse graining process in the transport model.

III. RESULTS AND DISCUSSION

At first, we can obtain the final-state particles in central collisions of isobaric Ru + Ru and Zr + Zr using the PACIAE model with CME. This simulation works on the assumption that (anti-)hyperons heavier than Λ ($\overline{\Lambda}$) have already decayed, and the model parameters are fixed on the default values given in the PYTHIA model, except the K factor and string fragmentation parameters parj(1), parj(2), and parj(3). These selected parameters are confirmed by roughly fitting production of p ($\overline{p}$) and Λ ($\overline{\Lambda}$) in 0%–15% ${}^{96}_{44}\mathrm{Ru}+{}^{96}_{44}\mathrm{Ru}$ and ${}^{96}_{40}\mathrm{Zr}+{}^{96}_{40}\mathrm{Zr}$ collisions to STAR data in 20%–40% centrality Au + Au collisions at $\sqrt{s_{\mathrm{NN}}}=200$ GeV, since their mean number of participating nucleons ($\langle N_{\mathrm{part}}\rangle$) are quite similar ≈140. Table I shows the corresponding integrated yields (dN/dy) of p and $\overline{p}$ with $|\eta|<0.1$ and $0.35<p_T<1.2$ GeV/c, as well as Λ and $\overline{\Lambda}$ within $|\eta|<0.5$ and $0.5<p_T<8.0$ GeV/c, respectively. p and $\overline{p}$ take into account of contributions from primordial Λ decays. For comparison, the STAR experimental data of 20%–40% Au + Au collisions [46,47] are also presented. It can be seen from Table I that the yields of particles (p, $\overline{p}$, Λ, and $\overline{\Lambda}$) in ${}^{96}_{44}\mathrm{Ru}+{}^{96}_{44}\mathrm{Ru}$ collision are the same as those of ${}^{96}_{40}\mathrm{Zr}+{}^{96}_{40}\mathrm{Zr}$ collisions at the specified collision centrality. Moreover, the results of the PACIAE model with CME for

TABLE I. The integrated yield dN/dy of particles (p, $\overline{p}$, Λ and $\overline{\Lambda}$) in 0%–15% centrality $^{96}_{44}$Ru + $^{96}_{44}$Ru and $^{96}_{40}$Zr + $^{96}_{40}$Zr collisions of $\sqrt{s_{\rm NN}} = 200$ GeV by PACIAE with CME, as compared with 20%–40% Au + Au collisions in STAR experimental data [46,47]. Here p ($\overline{p}$) are inclusive of contributions from primordial Λ ($\overline{\Lambda}$) decays.

Particle	PACIAE		STAR
type	Ru + Ru (0%–15%)	Zr + Zr (0%–15%)	Au + Au (20%–40%)
$\langle N_{\rm part}\rangle$	139.5 ± 1.4	139.5 ± 1.4	142.4 ± 5.3
p	11.13 ± 0.03	11.12 ± 0.03	11.85 ± 1.15
$\overline{p}$	9.60 ± 0.02	9.59 ± 0.01	9.33 ± 0.91
Λ	5.57 ± 0.02	5.55 ± 0.01	5.70 ± 0.55
$\overline{\Lambda}$	4.51 ± 0.01	4.50 ± 0.01	4.53 ± 0.34

the two isobaric nuclear collisions are well consistent with the measured STAR data for Au + Au collisions. The same fit parameters of $K = 3.0$, parj(1) = 0.13, parj(2) = 0.65, and parj(3) = 0.44 are chosen for these two isobaric nuclear collision systems.

Figure 1(a) presents the transverse momentum distributions of p ($\overline{p}$) and Λ ($\overline{\Lambda}$) (open symbols) in 0%–15% $^{96}_{44}$Ru + $^{96}_{44}$Ru and $^{96}_{40}$Zr + $^{96}_{40}$Zr collisions at $\sqrt{s_{\rm NN}} = 200$ GeV calculated by the PACIAE model with CME. The STAR experimental data for 20%–40% Au + Au collisions taken from Refs. [46,47] are shown by the solid symbols. It can be seen that the transverse momentum spectrum of particles p ($\overline{p}$) and Λ ($\overline{\Lambda}$) simulated by the PACIAE model with CME are compatible with the STAR data within uncertainties. Besides, Fig. 1(b) shows the distribution of the invariant yield ratios of particles for $^{96}_{44}$Ru + $^{96}_{44}$Ru and $^{96}_{40}$Zr + $^{96}_{40}$Zr collisions at $\sqrt{s_{\rm NN}} = 200$ GeV, as a function of p_T. Obviously, one can see from Fig. 1(b) that there is no significant difference for transverse momentum spectra of (anti-)particles between the two isobaric nuclear collisions, except the fluctuation at higher p_T.

In the following, we generate 4.0×10^8 most-central (0%–10%) events for $^{96}_{44}$Ru + $^{96}_{44}$Ru and $^{96}_{40}$Zr + $^{96}_{40}$Zr collisions at $\sqrt{s_{\rm NN}} = 200$ GeV using the PACIAE model with CME, respectively. These (anti-)nucleons and (anti-)hyperons produced within PACIAE with CME are used as input for the DCPC model. The proton productions from Λ feed down contribution is excluded in the coalescence procedure. Then, we obtain the integrated yields dN/dy of light (anti-)nuclei and (anti-)hypertriton nuclei with $|\eta| < 0.5$ and $p_T < 3.0$ GeV/c for the most-central bin of 0%–10%, respectively. Here we choose the parameter $\Delta m = 1.53$ MeV for $^3_\Lambda$H ($^3_{\overline{\Lambda}}\overline{\rm H}$), and $\Delta m = 2.13$ MeV for ^{3}He ($^3\overline{\rm He}$) and ^{3}H ($^3\overline{\rm H}$).

Table II presents the integrated yields dN/dy of (anti-)hyperons and (anti-)hypertriton (Λ, $\overline{\Lambda}$, $^3_\Lambda$H, $^3_{\overline{\Lambda}}\overline{\rm H}$), as well as (anti-)nuclei (p, $\overline{p}$, ^{3}He, $^3\overline{\rm He}$, ^{3}H, $^3\overline{\rm H}$) calculated by the PACIAE+DCPC model with CME in most central (0%–10%) $^{96}_{44}$Ru + $^{96}_{44}$Ru and $^{96}_{40}$Zr + $^{96}_{40}$Zr collisions at $\sqrt{s_{\rm NN}} =$ 200 GeV, respectively. It can be seen that the yields of (anti-)hypertriton, (anti-)tritium, and (anti-)helium-3 nuclei in central $^{96}_{44}$Ru + $^{96}_{44}$Ru and $^{96}_{40}$Zr + $^{96}_{40}$Zr collisions at $\sqrt{s_{\rm NN}} =$ 200 GeV from PACIAE + DCPC simulations are all at the order

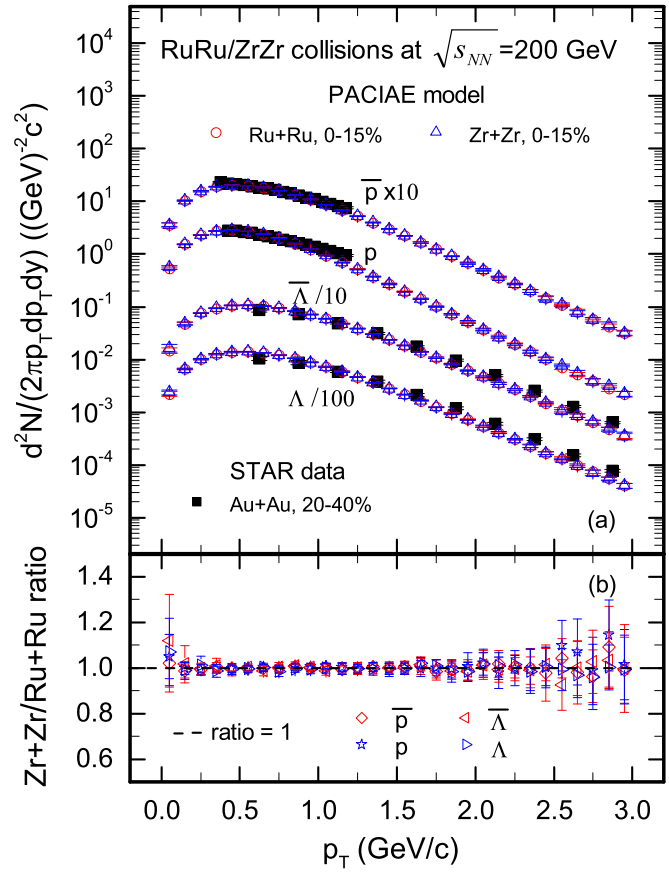

FIG. 1. (a) The transverse momentum spectrum of particles (p, $\overline{p}$, Λ, $\overline{\Lambda}$) in midrapidity $^{96}_{44}$Ru + $^{96}_{44}$Ru and $^{96}_{40}$Zr + $^{96}_{40}$Zr collisions at $\sqrt{s_{\rm NN}} = 200$ GeV. The open symbols show the results of PACIAE model with CME, and the solid symbols show the results from STAR data [46,47]. For clarity the spectra data are divided by powers of 10. (b) The yield ratios of particles (p, $\overline{p}$, Λ, $\overline{\Lambda}$) produced in $^{96}_{44}$Ru + $^{96}_{44}$Ru collisions to that in $^{96}_{40}$Zr + $^{96}_{40}$Zr collisions.

TABLE II. The integrated yields dN/dy of (anti-)particles p ($\overline{p}$), Λ ($\overline{\Lambda}$), and (anti-)nuclei $^3_\Lambda$H ($^3_{\overline{\Lambda}}\overline{\rm H}$), ^{3}He ($^3\overline{\rm He}$), ^{3}H ($^3\overline{\rm H}$) calculated by PACIAE + DCPC model with CME in 0%–10% $^{96}_{44}$Ru + $^{96}_{44}$Ru and $^{96}_{40}$Zr + $^{96}_{40}$Zr collisions of $\sqrt{s_{\rm NN}} = 200$ GeV with $|\eta| < 0.5$. Here p ($\overline{p}$) productions from Λ ($\overline{\Lambda}$) feed down contribution is excluded in the coalescence procedure.

Nucleus type	Ru + Ru (0%–10%)	Zr + Zr (0%–10%)
$\langle N_{\rm part}\rangle$	151.8 ± 1.4	151.8 ± 1.4
p	8.03 ± 0.02	8.02 ± 0.02
$\overline{p}$	6.51 ± 0.01	6.50 ± 0.03
Λ	7.04 ± 0.01	7.03 ± 0.01
$\overline{\Lambda}$	5.64 ± 0.01	5.65 ± 0.01
$^3_\Lambda$H (10^{-5})	6.50 ± 0.06	6.45 ± 0.07
$^3_{\overline{\Lambda}}\overline{\rm H}$ (10^{-5})	3.15 ± 0.03	3.12 ± 0.03
^{3}He (10^{-5})	8.57 ± 0.09	8.38 ± 0.08
$^3\overline{\rm He}$ (10^{-5})	4.41 ± 0.04	4.32 ± 0.04
^{3}H (10^{-5})	8.61 ± 0.08	8.51 ± 0.09
$^3\overline{\rm H}$ (10^{-5})	4.79 ± 0.04	4.73 ± 0.04

TABLE III. The (anti-)nucleus ratios from the PACIAE + DCPC model with CME in central (0%–10%) $^{96}_{44}$Ru + $^{96}_{44}$Ru and $^{96}_{40}$Zr + $^{96}_{40}$Zr collisions at $\sqrt{s_{\rm NN}} = 200$ GeV. The top section of the table shows the three ratios of antinucleus to nucleus, followed by the mixed ratios of (anti-)nucleus to (anti-)nucleus. The ratios between proton, antiproton, hyperon, and antihyperon are shown at the bottom. STAR data are taken from Cu + Cu and Au + Au collisions at $\sqrt{s_{\rm NN}} = 200$ GeV [6,46–49], respectively.

Nucleus	STAR		PACIAE + DCPC	
ratio	Cu + Cu	Au + Au	Ru + Ru	Zr + Zr
$^{3}_{\Lambda}\overline{\rm H}/^{3}_{\Lambda}$H		$0.49 \pm 0.18 \pm 0.07$	0.48 ± 0.02	0.48 ± 0.01
$^{3}\overline{\rm He}/^{3}$He	0.46 ± 0.17	$0.45 \pm 0.02 \pm 0.04$	0.51 ± 0.01	0.51 ± 0.01
$^{3}\overline{\rm H}/^{3}$H			0.56 ± 0.01	0.56 ± 0.01
$^{3}_{\Lambda}\overline{\rm H}/^{3}\overline{\rm He}$		$0.89 \pm 0.28 \pm 0.13$	0.71 ± 0.02	0.72 ± 0.01
$^{3}_{\Lambda}$H/^{3}He		$0.82 \pm 0.16 \pm 0.12$	0.76 ± 0.02	0.77 ± 0.01
$^{3}_{\Lambda}\overline{\rm H}/^{3}\overline{\rm H}$			0.66 ± 0.02	0.66 ± 0.01
$^{3}_{\Lambda}$H/^{3}H			0.75 ± 0.02	0.76 ± 0.02
$\overline{p}/p$	0.80 ± 0.04	0.79 ± 0.11	0.81 ± 0.01	0.81 ± 0.01
$\overline{\Lambda}/\Lambda$	0.82 ± 0.12	0.80 ± 0.10	0.80 ± 0.01	0.80 ± 0.01
Λ/p	0.84 ± 0.09		0.88 ± 0.01	0.88 ± 0.01
$\overline{\Lambda}/\overline{p}$	0.83 ± 0.08		0.87 ± 0.01	0.87 ± 0.01

of 10^{-5}. However, the yields of (anti-)hypernuclei are less than that of corresponding (anti-)nuclei with the equal baryon numbers. The yields of (anti-)hypernuclei and (anti-)nuclei in isobaric $^{96}_{44}$Ru + $^{96}_{44}$Ru and $^{96}_{40}$Zr + $^{96}_{40}$Zr collisions are the same within the range of uncertainty, indicating that the production of (anti-)hypernuclei and light (anti-)nuclei between the two isobaric nuclei-nuclei collisions is insensitive to the difference in charge.

To understand the fundamental properties of antimatter in nuclear collisions, we provide a systematic investigation to the yield ratios of different (anti-)nuclei and (anti-)hypernuclei, which are deeply related to the fractions of constituent nucleons in the naive coalescence framework [11,15]. For instance, the yield ratio of $^{3}_{\Lambda}\overline{\rm H}/^{3}_{\Lambda}$H should be proportional to $(\overline{p}/p)(\overline{n}/n)(\overline{\Lambda}/\Lambda)$, which is approximate to $(\overline{p}/p)^2(\overline{\Lambda}/\Lambda)$, i.e,

$$\frac{^{3}_{\Lambda}\overline{\rm H}}{^{3}_{\Lambda}{\rm H}} = \frac{\overline{\rm pn}\overline{\Lambda}}{\rm pn\Lambda} \simeq \left(\frac{\overline{\rm p}}{\rm p}\right)^2 \frac{\overline{\Lambda}}{\Lambda}. \tag{7}$$

Table III represents the yield ratios of antiparticles to particles ($\overline{p}/p$, $\overline{\Lambda}/\Lambda$, $^{3}_{\Lambda}\overline{\rm H}/^{3}_{\Lambda}$H, $^{3}\overline{\rm He}/^{3}$He, $^{3}\overline{\rm H}/^{3}$H), and the mixed ratios ($\overline{\Lambda}/\overline{p}$, Λ/p, $^{3}_{\Lambda}\overline{\rm H}/^{3}\overline{\rm He}$, $^{3}_{\Lambda}$H/^{3}He, $^{3}_{\Lambda}\overline{\rm H}/^{3}\overline{\rm H}$, $^{3}_{\Lambda}$H/^{3}H) calculated by PACIAE + DCPC model with CME in $^{96}_{44}$Ru + $^{96}_{44}$Ru and $^{96}_{40}$Zr + $^{96}_{40}$Zr collisions at $\sqrt{s_{\rm NN}} = 200$ GeV. One can see from Table III that the yield ratios of $^{3}_{\Lambda}\overline{\rm H}/^{3}_{\Lambda}$H, $^{3}\overline{\rm He}/^{3}$He, and $^{3}\overline{\rm H}/^{3}$H are the same within the error range, although their yields are not the same as shown in Table II. And the mixed ratio values of (anti-)hypernuclei to (anti-)nuclei($^{3}_{\Lambda}\overline{\rm H}/^{3}\overline{\rm He}$, $^{3}_{\Lambda}$H/^{3}He, $^{3}_{\Lambda}\overline{\rm H}/^{3}\overline{\rm H}$, $^{3}_{\Lambda}$H/^{3}H) are also the same in the range of uncertainty in central isobaric Ru + Ru and Zr + Zr at $\sqrt{s_{\rm NN}} = 200$ GeV. Besides, the yield ratio results of antiparticles to particles and their mixed ratios simulated by the PACIAE + DCPC model with CME are found to be in agreement with the above theoretical interpretation within uncertainties.

Figure 2 and Table III show that the ratios of antinuclei to nuclei ($^{3}_{\Lambda}\overline{\rm H}/^{3}_{\Lambda}$H, $^{3}\overline{\rm He}/^{3}$He, $^{3}\overline{\rm H}/^{3}$H) are less than 1, meaning that the yields of antiparticles is less than that of corresponding particles; similarly, the mixed ratio values indicate that the yields of the (anti-)hypertriton are less than that of (anti-)nuclei. Our simulation results are consistent with the STAR data of Cu + Cu [46,48,49] and Au + Au [6,46,47] collisions at $\sqrt{s_{\rm NN}} = 200$ GeV.

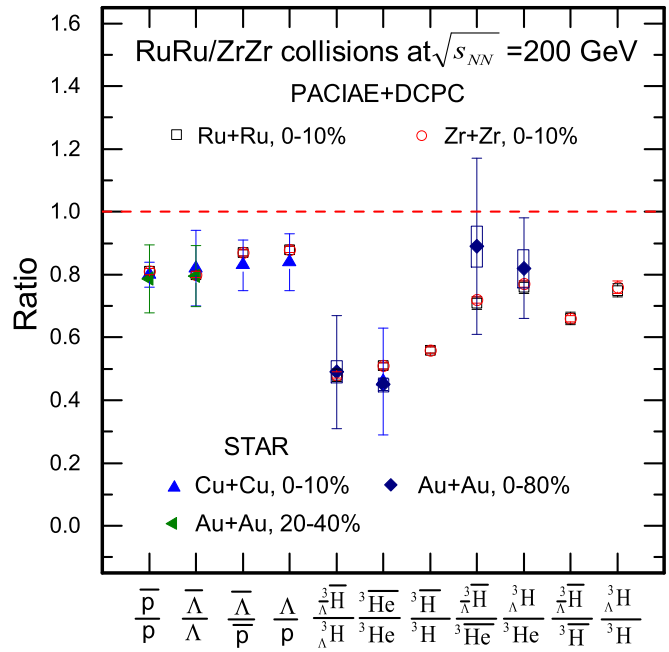

FIG. 2. The ratios and mixed ratios of (anti-)matter form PACIAE + DCPC model with CME (open symbols) in 0%–10% Ru + Ru and Zr + Zr collisions, compared with Cu + Cu and Au + Au collisions. The data are taken from STAR [6,46–49]. The vertical lines and error boxes show statistical and systematic errors, respectively.

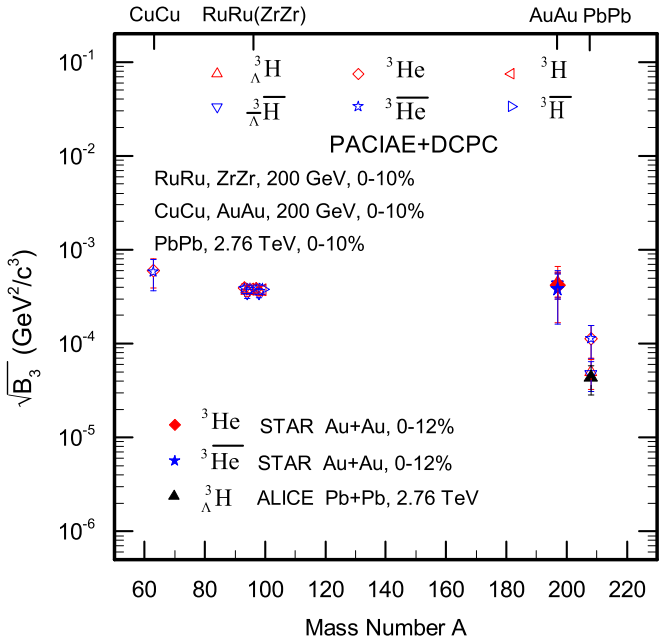

FIG. 3. The coalescence parameters $\sqrt{B_3}$ of ${}^3_\Lambda\mathrm{H}({}^3_\Lambda\overline{\mathrm{H}})$, as well as ${}^3\mathrm{H}({}^3\overline{\mathrm{H}})$ and ${}^3\mathrm{He}({}^3\overline{\mathrm{He}})$ are compared in isobars ${}^{96}_{44}\mathrm{Ru}+{}^{96}_{44}\mathrm{Ru}$ and ${}^{96}_{40}\mathrm{Zr}+{}^{96}_{40}\mathrm{Zr}$ collisions at $\sqrt{s_{\mathrm{NN}}}=200$ GeV with the PACIAE+ DCPC model with CME. It is also compared with the results from different collisions of Cu + Cu [38], Au + Au [42], and Pb + Pb [43] collisions. The open symbols denote the results computed by PACIAE+ DCPC. The solid points take from STAR [50] and ALICE [7]. The error bars show statistical uncertainties.

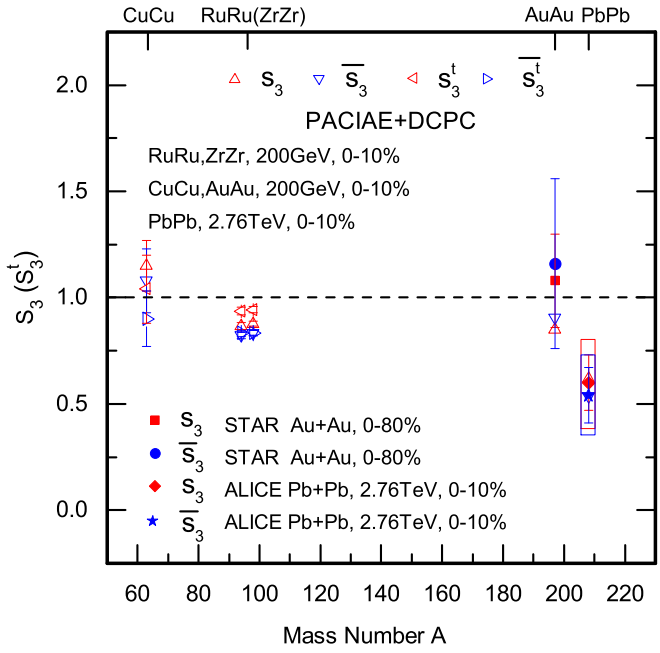

FIG. 4. Comparison of strangeness population factor $s_3(s_3^t)$ in isobars ${}^{96}_{44}\mathrm{Ru}+{}^{96}_{44}\mathrm{Ru}$ and ${}^{96}_{40}\mathrm{Zr}+{}^{96}_{40}\mathrm{Zr}$ collisions at $\sqrt{s_{\mathrm{NN}}}=200$ GeV by PACIAE + DCPC model with CME. It is also compared with the results of Cu + Cu [20], Au + Au [42], and Pb + Pb [43] collisions. The open symbols denote the results computed by PACIAE + DCPC, and the solid points denote data from STAR [6] and ALICE [7]. Error bars and error boxes denote statistical and systematic errors, respectively.

In nuclear collisions, the invariant yields for production of (anti-)hypernuclei and (anti-)nuclei can be related to the primordial yields of (anti-)nucleons in the coalescence framework [51,52] by

$$E_A\frac{d^3N_A}{d^3P_A}\approx B_A\left(E_P\frac{d^3N_P}{d^3P_P}\right)^A, \tag{8}$$

where Ed^3N/d^3p stands for the invariant yields of nucleons or light (anti-)nuclei and (anti-)hypernuclei, and A is the atomic mass number, respectively. B_A represents the coalescence parameters, which relates to the freeze-out correlation volume, i.e., $B_A\propto V_f^{1-A}$. p_A, p_p denote their momentum, with $p_A=Ap_p$ assumed.

Figure 3 presents coalescence parameters $\sqrt{B_3}$ of ${}^3_\Lambda\mathrm{H}$ $({}^3_\Lambda\overline{\mathrm{H}})$, as well as ${}^3\mathrm{He}$ $({}^3\overline{\mathrm{He}})$ and ${}^3\mathrm{H}$ $({}^3\overline{\mathrm{H}})$ in Ru + Ru and Zr + Zr collisions. Meanwhile, the results from different collision systems of Cu + Cu [20], Au + Au [42], and Pb + Pb [43] collisions are compared as a function of atomic mass number A. One can see that $\sqrt{B_3}$ calculated by PACIAE + DCPC model with CME is constant within the error range from Cu + Cu ($A=63$) to Au + Au ($A=197$) collisions at top RHIC energy. The coalescence parameter is found to drop from RHIC energy to PbPb collisions at the LHC energy. This decreasing can be understood as the correlation volume of the QGP fireball at LHC becomes larger, as indicated by the pion HBT measurement [42,50].

Specifically, with respect to 0%–10% Ru + Ru or Zr + Zr collisions, the values of $\sqrt{B_3}$ for nuclei ${}^3_\Lambda\mathrm{H}$, ${}^3\mathrm{He}$, ${}^3\mathrm{H}$ and their corresponding antinuclei ${}^3_\Lambda\overline{\mathrm{H}}$, ${}^3\overline{\mathrm{He}}$, ${}^3\overline{\mathrm{H}}$ are about $(3.63\pm0.46)\times10^{-4}$, $(3.90\pm0.42)\times10^{-4}$, $(3.79\pm0.39)\times10^{-4}$ and $(3.46\pm0.44)\times10^{-4}$, $(3.81\pm0.40)\times10^{-4}$, $(3.75\pm0.41)\times10^{-4}$, respectively. It is clear that the value of $\sqrt{B_3}$ of the (anti-)hypertriton is the same as that of the (anti-)nuclei within the uncertainties. One can also find that the negative (hyper-)nuclei are the same as the positive (hyper-)nuclei. Meanwhile, the experiment data of 0%–12% Au + Au in STAR [50] and 0%–10% Pb + Pb from ALICE [7] are also presented in Fig. 3.

The strangeness population factor s_3, should be about one in the coalescence model for particle production, as first suggested in Ref. [21]. It is a possible tool to study the nature of a quark-gluon plasma created in high-energy nuclear collisions [53], due to its sensitivity to the local baryon-strangeness correlation [54,55]. This factor typically is written as

$$s_3=\left({}^3_\Lambda\mathrm{H}\times p\right)/\left({}^3\mathrm{He}\times\Lambda\right), \tag{9}$$

which can be straightforwardly extended to ${}^3\mathrm{H}$ expressed as

$$s_3^t=\left({}^3_\Lambda\mathrm{H}\times p\right)/\left({}^3\mathrm{H}\times\Lambda\right). \tag{10}$$

In Fig. 4, we compare the values of strangeness population factor $s_3(\overline{s_3})$ and $s_3^t(\overline{s_3^t})$ calculated by PACIAE + DCPC model with CME in central Ru + Ru and Zr + Zr collisions. Besides, the values of Cu + Cu [20], Au + Au [42], and Pb + Pb [43]

collisions varying with mass number A are also presented in this figure. It is shown that the values of $s_3(\overline{s_3})$ and $s_3^t(\overline{s_3^t})$ for three-body coalescence are all the same within the error range as A increases from 63 to 197 in central (0%–10%) Cu + Cu, Ru + Ru (Zr + Zr) to Au + Au collisions at RHIC energy. But the values of $s_3(\overline{s_3})$ and $s_3^t(\overline{s_3^t})$ decrease in Pb + Pb collisions at $\sqrt{s_{\rm NN}} = 2.76$ TeV. This may be interpreted as the (anti-)Λ particles freeze-out earlier than (anti-)nucleons but their relative freeze-out time is closer at the LHC than at RHIC [18].

Numerically, the present values of $s_3, \bar{s}_3$ and $s_3^t, \overline{s_3^t}$ are $0.87 \pm 0.02, 0.82 \pm 0.02$ and $0.94 \pm 0.02, 0.83 \pm 0.02$ in 0%–10% Ru + Ru collisions, and $0.88 \pm 0.01, 0.83 \pm 0.01$ and $0.94 \pm 0.02, 0.83 \pm 0.02$ in 0%–10% Zr + Zr collisions, respectively. Meanwhile, the values of $s_3(\overline{s_3})$ and $s_3^t(\overline{s_3^t})$ shown in the Fig. 4 for Au + Au and Pb + Pb collisions by PACIAE + DCPC model are in agreement with the corresponding available data from STAR [6] and ALICE [7] within uncertainties.

IV. CONCLUSION

In this paper, we use the PACIAE model with CME and DCPC model to simulate the production of ${}^3_\Lambda$H and ${}^3_\Lambda\overline{\rm H}$, as well as ^{3}H, ${}^3\overline{\rm H}$, ^{3}He, and ${}^3\overline{\rm He}$ in isobaric ${}^{96}_{44}$Ru + ${}^{96}_{44}$Ru and ${}^{96}_{40}$Zr + ${}^{96}_{40}$Zr central collisions at $\sqrt{s_{\rm NN}} = 200$ GeV with $|\eta| < 0.5$ and $p_T < 3.0$ GeV/c, respectively. We predict the yield, yield ratio, coalescence parameters, and strangeness population factor of (anti-)hypertriton (${}^3_\Lambda$H, ${}^3_\Lambda\overline{\rm H}$) and (anti-)nuclei (^{3}H, ${}^3\overline{\rm H}$, ^{3}He, ${}^3\overline{\rm He}$) in isobaric Ru + Ru and Zr + Zr collisions. Then the chiral magnetic effect on the generation of (anti-)hypertriton (${}^3_\Lambda$H, ${}^3_\Lambda\overline{\rm H}$) and (anti-)nuclei (^{3}H, ${}^3\overline{\rm H}$, ^{3}He, ${}^3\overline{\rm He}$) in high-energy collisions are studied. It is found that there is no clear difference for the generation and properties of (anti-)hypertriton (${}^3_\Lambda$H, ${}^3_\Lambda\overline{\rm H}$) and light (anti-)nuclei (^{3}H, ${}^3\overline{\rm H}$, ^{3}He, ${}^3\overline{\rm He}$) in isobaric Ru + Ru and Zr + Zr collision systems, although these two collision systems have different CME.

In addition, the coalescence parameters $\sqrt{B_3}$ and the strangeness population factor $s_3(s_3^t)$ that produce ${}^3_\Lambda$H(${}^3_\Lambda\overline{\rm H}$), as well as ^{3}H(${}^3\overline{\rm H}$) and ^{3}He(${}^3\overline{\rm He}$) in ${}^{96}_{44}$Ru + ${}^{96}_{44}$Ru and ${}^{96}_{40}$Zr + ${}^{96}_{40}$Zr collisions are compared with those of Cu + Cu, Au + Au, and Pb + Pb collisions at $\sqrt{s_{\rm NN}} = 200$ GeV by the PACIAE + DCPC model. One can see that the $\sqrt{B_3}$ and $s_3(s_3^t)$ are all the same within the error range as atomic mass number A increases from 63 to 197 in Cu + Cu, Ru + Ru (Zr + Zr) to Au + Au collisions at RHIC energy. But the values of $s_3(\overline{s_3})$ and $s_3^t(\overline{s_3^t})$ decrease in Pb + Pb collisions at $\sqrt{s_{\rm NN}} = 2.76$ TeV. This may be interpreted as the Λ ($\overline{\Lambda}$) particles freeze-out earlier than (anti-)nucleons but their relative freeze-out time is closer at the LHC than at RHIC. The experimental data of Cu + Cu, Au + Au and Pb + Pb collisions from RHIC, LHC are included in the comparison, which shows that our simulation results for the $\sqrt{B_3}$ and $s_3(s_3^t)$ of ${}^3_\Lambda$H (${}^3_\Lambda\overline{\rm H}$), ^{3}He (${}^3\overline{\rm He}$), ^{3}H (${}^3\overline{\rm H}$) are consistent with the experimental results within the error range.

ACKNOWLEDGMENTS

This work was supported by the National Natural Science Foundation of China under Grants No. 11475149, No. 11775094, and No. 11905188, as well as supported by the high-performance computing platform of China University of Geosciences. The authors thank Dr. Feng-Xian Liu for fruitful discussions.

[1] J. H. Chen, D. Keane, Y. G. Ma *et al.*, Phys. Rep. **760**, 1 (2018).
[2] Y. G. Ma, J. H. Chen, and L. Xue, Front. Phys. **7**, 637 (2012).
[3] P. Braun-Munzinger and B. Dönigus, Nucl. Phys. A **987**, 144 (2019).
[4] J. Adam *et al.* (STAR Collaboration), Nat. Phys. **16**, 409 (2020).
[5] S. Acharya *et al.* (ALICE Collaboration), Phys. Lett. B **797**, 134905 (2019).
[6] B. I. Abelev *et al.* (STAR Collaboration), Science **328**, 58 (2010).
[7] J. Adam *et al.* (ALICE Collaboration), Phys. Lett. B **754**, 360 (2016).
[8] E. Botta, T. Bressani, and G. Garbarino, Eur. Phys. J. A **48**, 41 (2012).
[9] V. Topor Pop and S. Das Gupta, Phys. Rev. C **81**, 054911 (2010).
[10] A. Andronic, P. Braun-Munzinger, J. Stachel *et al.*, Phys. Lett. B **697**, 203 (2011).
[11] J. Cleymans, S. Kabana, I. Kraus, H. Oeschler, K. Redlich, and N. Sharma, Phys. Rev. C **84**, 054916 (2011).
[12] S. Pal and W. Greiner, Phys. Rev. C **87**, 054905 (2013).
[13] S. Chatterjee and B. Mohanty, Phys. Rev. C **90**, 034908 (2014).
[14] A. Andronic, P. Braun-Munzinger, K. Redlich *et al.*, Nature (London) **561**, 321 (2018).
[15] L. Xue, Y. G. Ma, J. H. Chen, and S. Zhang, Phys. Rev. C **85**, 064912 (2012).
[16] L. L. Zhu, C. M. Ko, and X. J. Yin, Phys. Rev. C **92**, 064911 (2015).
[17] N. Shah, Y. G. Ma, J. H. Chen *et al.*, Phys. Lett. B **754**, 6 (2016).
[18] K. J. Sun and L. W. Chen, Phys. Rev. C **93**, 064909 (2016).
[19] P. Liu, J. H. Chen, Y. G. Ma, and S. Zhang, Nucl. Sci. Tech. **28**, 55 (2017).
[20] F. X. Liu, G. Chen, Z. L. She *et al.*, Phys. Rev. C **99**, 034904 (2019).
[21] T. Armstrong *et al.* (E864 Collaboration), Phys. Rev. C **70**, 024902 (2004).
[22] Y. F. Sun and C. M. Ko, Phys. Rev. C **98**, 014911 (2018).
[23] H. J. Xu, X. B. Wang, H. L. Li, J. Zhao, Z. W. Lin, C. Shen, and F. Wang, Phys. Rev. Lett. **121**, 022301 (2018).
[24] X. L. Zhao, G. L. Ma, and Y. G. Ma, Phys. Rev. C **99**, 034903 (2019).
[25] J. Adam *et al.* (STAR Collaboration), arXiv:1911.00596.
[26] J. Zhao and F. Q. Wang, Prog. Part. Nucl. Phys. **107**, 200 (2019).

[27] G. L. Ma and B. Zhang, Phys. Lett. B **700**, 39 (2011).
[28] W. T. Deng, X. G. Huang, G. L. Ma, and G. Wang, Phys. Rev. C **97**, 044901 (2018).
[29] L. Huang, C. W. Ma, and G. L. Ma, Phys. Rev. C **97**, 034909 (2018).
[30] L. Huang, M. W. Nie, and G. L. Ma, Phys. Rev. C **101**, 024916 (2020).
[31] Z. W. Lin, C. M. Ko, B. A. Li, B. Zhang, and S. Pal, Phys. Rev. C **72**, 064901 (2005).
[32] B. H. Sa, D. M. Zhou, Y. L. Yan *et al.*, Comput. Phys. Commun. **183**, 333 (2012).
[33] Y. L. Yan, G. Chen, X. M. Li *et al.*, Phys. Rev. C **85**, 024907 (2012).
[34] T. Sjöstrand, S. Mrenna, and P. Skands, J. High Energy Phys. 05 (2006) 026.
[35] B. L. Combridge, J. Kripfgang, and J. Ranft, Phys. Lett. B **70**, 234 (1977).
[36] J. L. Wang, D. K. Li, H. J. Li *et al.*, Int. J. Mod. Phys. E **23**, 1450088 (2014).
[37] N. A. Ragab, Z. L. She, and G. Chen, Eur. Phys. J. Plus **135**, 736 (2020).
[38] F. X. Liu, G. Chen, Z. L. She *et al.*, Eur. Phys. J. A **55**, 160 (2019).
[39] G. Chen, Y. L. Yan, D. S. Li, D. M. Zhou, M. J. Wang, B. G. Dong, and B. H. Sa, Phys. Rev. C **86**, 054910 (2012).
[40] G. Chen, H. Chen, J. Wu, D. S. Li, and M. J. Wang, Phys. Rev. C **88**, 034908 (2013).
[41] G. Chen, H. Chen, J. L. Wang *et al.*, J. Phys. G **41**, 115102 (2014).
[42] Z. J. Dong, Q. Y. Wang, G. Chen *et al.*, Eur. Phys. J. A **54**, 144 (2018).
[43] Z. L. She, G. Chen, H. G. Xu *et al.*, Eur. Phys. J. A **52**, 93 (2016).
[44] Z. L. She, G. Chen, D. M. Zhou *et al.*, arXiv:1909.07070.
[45] H. Nemura, Y. Suzuki, Y. Fujiwara *et al.*, Prog. Theor. Phys. **103**, 929 (2000).
[46] G. Agakishiev *et al.* (STAR Collaboration), Phys. Rev. Lett. **108**, 072301 (2012).
[47] B. I. Abelev *et al.* (STAR Collaboration), Phys. Rev. C **79**, 034909 (2009).
[48] M. M. Aggarwal *et al.* (STAR Collaboration), Phys. Rev. C **83**, 034910 (2011).
[49] J. Zhou, Light (anti-)nuclei production in the STAR experiment at RHIC, Ph.D. thesis, Rice University, 2009 (unpublished).
[50] B. I. Abelev *et al.* (STAR Collaboration), arXiv:0909.0566.
[51] R. Scheibl and U. Heinz, Phys. Rev. C **59**, 1585 (1999).
[52] H. H. Gutbrod, A. Sandoval, P. J. Johansen *et al.*, Phys. Rev. Lett. **37**, 667 (1976).
[53] S. Zhang, J. H. Chen, H. Crawford *et al.*, Phys. Lett. B **684**, 224 (2010).
[54] V. Koch, A. Majumder, and J. Randrup, Phys. Rev. Lett. **95**, 182301 (2005).
[55] J. Steinheimer, K. Gudima, A. Botvina *et al.*, Phys. Lett. B **714**, 85 (2012).